

## Optically Induced Anisotropy in Time-Resolved Scattering: Imaging Molecular-Scale Structure and Dynamics in Disordered Media with Experiment and Theory

Andrés Montoya-Castillo<sup>1</sup>,<sup>✉</sup> Michael S. Chen,<sup>2</sup> Sumana L. Raj<sup>3</sup>,<sup>✉</sup> Kenneth A. Jung,<sup>2</sup> Kasper S. Kjaer,<sup>3</sup> Tobias Morawietz,<sup>2</sup> Kelly J. Gaffney<sup>3,\*</sup>, Tim B. van Driel<sup>4,†</sup>, and Thomas E. Markland<sup>2,‡</sup>

<sup>1</sup>*Department of Chemistry, University of Colorado, Boulder, Colorado 80309, USA*

<sup>2</sup>*Department of Chemistry, Stanford University, Stanford, California 94305, USA*

<sup>3</sup>*Stanford PULSE Institute, SLAC National Accelerator Laboratory, Stanford University, Menlo Park, California 94025, USA*

<sup>4</sup>*Linac Coherent Light Source, SLAC National Accelerator Laboratory, Menlo Park, California 94025, USA*



(Received 4 February 2022; accepted 29 June 2022; published 29 July 2022)

Time-resolved scattering experiments enable imaging of materials at the molecular scale with femtosecond time resolution. However, in disordered media they provide access to just one radial dimension thus limiting the study of orientational structure and dynamics. Here we introduce a rigorous and practical theoretical framework for predicting and interpreting experiments combining optically induced anisotropy and time-resolved scattering. Using impulsive nuclear Raman and ultrafast x-ray scattering experiments of chloroform and simulations, we demonstrate that this framework can accurately predict and elucidate both the spatial and temporal features of these experiments.

DOI: [10.1103/PhysRevLett.129.056001](https://doi.org/10.1103/PhysRevLett.129.056001)

The characterization of the structure and dynamics of disordered media ranging from liquids to solutions and glasses with atomic resolution remains a formidable challenge. Whether using x rays, neutrons, or electrons to characterize the structure of these systems the orientational averaging associated with isotropic samples reduces the structural information to a single radial dimension inhibiting the ability to resolve the orientational structure and dynamics.

The situation becomes even more vexing when the goal extends to understanding the dynamics of liquids and solutions with atomic resolution. Accessing this information requires techniques that can probe timescales from tens of femtoseconds to hundreds of picoseconds corresponding to frequencies ranging from  $\sim 0.1$  to  $\sim 1,000$   $\text{cm}^{-1}$ . While ultrafast nonlinear spectroscopies can be used to investigate dynamics in this temporal range, they do not provide a direct link to the underlying structural changes occurring, necessitating their combination with other techniques, such as simulation, to infer these connections [1]. In contrast, inelastic x-ray and neutron scattering measurements provide access to the required spatial resolution, but in practice the low count rates of the measurements limit their impact [2–4].

The advent of intense ultrafast x-ray laser sources has enabled the combination of ultrafast nonlinear optical excitation methods and x-ray scattering to access the dynamics of liquids and solutions in the femtosecond temporal and Ångström spatial dimensions [5–8]. In particular, impulsive nuclear Raman and x-ray scattering (INXS) combines nonresonant impulsive stimulated Raman scattering (ISRS) interactions, which excite

Raman active vibrational and rotational motions [9–11] and generate nonequilibrium nuclear geometries, with ultrafast time-resolved elastic x-ray scattering to probe these structural dynamics [12,13]. INXS has recently been experimentally realized [12,13] and offers the potential to obtain radial and orientational structure and dynamics of liquids on the Ångström to nanometer length scale and the femtosecond to picosecond timescale. By generating changes in both the radial and orientational order of disordered media, ISRS interactions can generate both isotropic and anisotropic changes in the structure factor, thus extending radial information present in INXS to a second spatial (orientational) dimension. These developments thus present a tremendous opportunity for combining optically induced anisotropic excitations with nuclear scattering probes such as ISRS with x-ray scattering to transform our understanding of the structure and dynamics of disordered media.

To elucidate and harness the rich information present in experiments which exploit the combination of optically induced anisotropy and time-resolved scattering and inspire future developments, it is essential to develop quantitatively predictive theories that can reproduce experimental signals and provide an interpretational framework of these cutting edge measurements. Specifically, a theory of INXS experiments, which can now be readily performed at x-ray free electron laser sources, that can quantitatively capture the experimentally observed signals has yet to be realized. Here we derive a rigorous and practical quantum mechanical framework in the linear response limit for predicting and interpreting experiments involving optically induced anisotropy

combined with time-resolved scattering. By performing INXS experiments of liquid chloroform and simulations of our theory based on a polarizable force field [14], we show that our approach provides a quantitative description of the INXS signal and thus provides a robust and clear foundation for understanding and interpreting INXS experiments that can be extended to other liquids and solutions.

From both a theoretical and interpretational perspective, the linear response formulation [1] offers numerous advantages. By employing this formulation we cast the system's nonequilibrium response to light-matter interactions in terms of equilibrium time correlation functions, which allows one to elucidate a system's inherent response rather than one that depends on the details of the nonequilibrium simulation designed to mirror the physical process being probed. This formulation incorporates the optical and x-ray pulses through a convolution with the system's inherent response, allowing one to also study the effect of pulse shaping on the signal. When taken to the classical limit of the nuclei, our approach permits the use of the well developed toolbox of atomistic simulation techniques to simulate the INXS signal.

To formulate our theory, we consider the features of the INXS experiment. INXS initially pumps the sample with an electronically and vibrationally off resonant optical pulse and then probes it with an off resonant x-ray pulse, leading to a time-resolved scattering pattern on the detector plane (Supplemental Material, Fig. 1 [15]). The frequency dependence of the INXS signal recovers Raman active modes (see Fig. 2). Hence, INXS is a third-order nonlinear scattering method with the initial interaction consisting of an optical Raman excitation followed by a scattering interaction [12,13].

We thus employ an expansion of the system's density matrix to third order in the light-matter coupling [1,16] subject to the INXS sequence of excitation and scattering interactions. In the Supplemental Material, Sec. I [15], we first derive a rigorous quantum mechanical expression for the INXS signal and then demonstrate how INXS experiments permit a series of well-controlled approximations [1,16–42] that result in an expression for the INXS signal at time  $t$  after the initial excitation that is compatible with direct atomistic simulations,

$$\Delta S(\mathbf{q}_{xy}, t) = \mathcal{N}^{\text{clas}} \int_0^t d\tau |E_{\text{opt}}(t - \tau)|^2 \mathcal{R}(\mathbf{q}_{xy}, \tau), \quad (1)$$

where  $\mathcal{N}^{\text{clas}}$  is given in Eq. (3),  $E_{\text{opt}}(t)$  is the electric field envelope for the optical interaction, and

$$\mathcal{R}(\mathbf{q}_{xy}, t) = \frac{d}{dt} \langle \tilde{\alpha}(0, \{\mathbf{R}\}) \Sigma(\mathbf{q}_{xy}, t) \rangle_{\text{eq}}. \quad (2)$$

Here  $\mathcal{R}(\mathbf{q}_{xy}, t)$  is the INXS response function in the limit of classical nuclei [for the quantum mechanical expression,

see Supplemental Material, Eq. (37) [15]] that correlates the Raman excitation at  $t = 0$ , given by the linear combination of polarizability tensor elements, with the x-ray scattering pattern at time  $t$ , given by the  $x - y$  cut (perpendicular to the  $z$ -propagation direction of the incoming x-ray probe) of the x-ray scattering operator,  $\Sigma(\mathbf{q}_{xy})$ . While our expression can be combined with a range of methods to treat  $\Sigma(\mathbf{q}_{xy})$ , in our simulations below we employ the widely adopted independent atom model [29,32].

An immediate success of our expression for the INXS signal, Eq. (1), lies in the derived proportionality constant,

$$\mathcal{N}^{\text{clas}} = - \frac{\beta(\mathbf{e}_{\text{xr}} \cdot \mathbf{e}_s)^2 |E_{\text{xr}}|^2 |E_s|^2}{\omega_{\text{opt}}^2 \omega_s^2 \omega_{\text{xr}}^2} \quad (3)$$

which offers testable predictions of the scaling of the INXS signal with respect to the experimental setup and strengths and frequencies of the light pulses. In particular,  $\mathcal{N}^{\text{clas}}$  predicts that the INXS signal is strongest when the incoming and scattered x ray are collinearly polarized, ( $\mathbf{e}_{\text{xr}} \cdot \mathbf{e}_s = 1$ ), and diminishes to zero when perpendicular ( $\mathbf{e}_{\text{xr}} \cdot \mathbf{e}_s = 0$ ). It also depends quadratically on the magnitude of the electric field for the optical ( $E_{\text{opt}}$ ) and incoming ( $E_{\text{xr}}$ ) and scattered ( $E_s$ ) x-ray pulses, and is inversely proportional to the square of the frequencies for the optical ( $\omega_{\text{opt}}$ ) and incoming ( $\omega_{\text{xr}}$ ) and scattered ( $\omega_s$ ) x-ray pulses. Our experiments have confirmed all these predictions, providing support for applicability of our linear response theory treatment of the INXS interactions.

A fundamental question that arises in the theoretical treatment of the INXS experiment is when an anisotropic INXS signal will emerge from a homogeneous and isotropic system. Equation (2) shows that the anisotropic signal can be captured from the correlations of the instantaneous fluctuations of the polarizability tensor and cuts of the structure factor of the fully isotropic system at equilibrium. In particular, Eq. (2) correlates the components of the polarizability tensor,  $\alpha_{\mathbf{e}_{\text{opt}}}(\{\mathbf{R}\})$ , that depend on the global nuclear configuration,  $\{\mathbf{R}\}$ , and the  $x - y$  cut of the modified structure factor,  $\mathbf{q}_{xy} = q_x \hat{\mathbf{x}} + q_y \hat{\mathbf{y}}$ , that arises from a constrained Fourier transform ( $q_z = 0$ ) of the microscopic positions of all atoms in the system. Equation (2) also shows that systems characterized by a global (i.e., of the entire sample rather than of individual molecules) isotropic polarizability tensor,  $\alpha_{xx} = \alpha_{yy} = \alpha_{zz}$  and  $\alpha_{jk} = 0$  where  $j \neq k \in \{x, y, z\}$ , can only produce isotropic INXS signals. This is because the polarization of the optical pulse, whether it is linearly or circularly polarized, sets the linear combination of the polarizability tensor elements in Eq. (2) [Supplemental Material Eq. (33) [15]]. For instance, an optical pulse linearly polarized at an angle  $\phi$  with respect to the  $x - y$  plane,  $\mathbf{e}_{\text{opt}} = \hat{\mathbf{x}} \cos(\phi) + \hat{\mathbf{y}} \sin(\phi)$ , as is the case in our

experiment (see Supplemental Material, Fig. 1 [15]), leads to  $\tilde{\alpha} = \cos^2(\phi)\alpha_{xx} + \sin^2(\phi)\alpha_{yy} + \sin(\phi)\cos(\phi)(\alpha_{xy} + \alpha_{yx})$ . As such, when  $\alpha_{xx} = \alpha_{yy}$  and  $\alpha_{xy} = 0 = \alpha_{yx}$ , the resulting INXS signal would have no  $\phi$  dependence on the detector plane and therefore no anisotropic component. Hence, the anisotropy of the INXS signal arises from the filtering of the wave-vector-restricted structure factor  $\Sigma(\mathbf{q}_{xy})$  imposed by the anisotropy of the polarizability tensor  $\alpha_{\epsilon_{\text{opt}}}(\{\mathbf{R}\})$  of the entire system which depends on the global nuclear configuration of the sample. As the experimental and simulation results below demonstrate, the INXS signal provides an avenue to break the symmetry of an x-ray scattering pattern as filtered through the nuclear position-dependent polarizability tensor and analyze how its time evolution reveals the connection between structural rearrangements and energy relaxation pathways in complex liquids.

To assess the ability of our theoretical approach to understand and interpret INXS we performed INXS experiments of chloroform (Supplemental Material, Sec. II, [15,43–45]). The top row of Fig. 1 compares the difference INXS signal  $\Delta S(q, t)$ , relative to the equilibrium elastic x-ray scattering signal, measured at times from 28 fs to 352 fs after excitation. This signal exhibits strong anisotropy that increases for the first 200 fs, followed by a decay over the next few picoseconds that leaves an

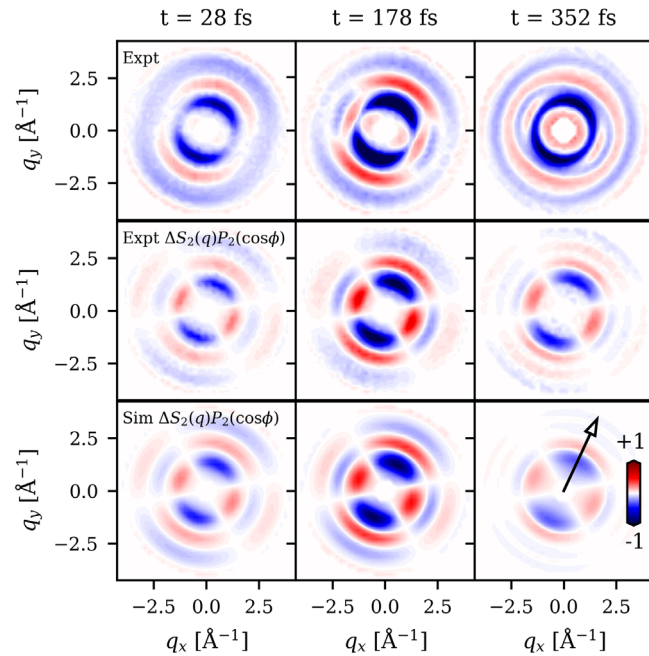


FIG. 1. The experimental difference INXS signal (top, see Supplemental Material, Fig. 6 [15], for raw signal) and anisotropic component,  $\Delta S_2(q, t)P_2(\cos\phi)$ , of the signal obtained from experiment (middle) and theory (bottom) at times  $t$  following the initial excitation of the sample. The arrow in the lower right panel defines the direction of the optical excitation electronic field.

isotropic background signal due to an increase in liquid temperature of  $\sim 18$  K arising from the pump excitation (Supplemental Material, Sec. IIC [15,45] and Supplemental Material, Fig. 2 [15]). The prominent anisotropic nature of the signal highlights the utility of this approach in obtaining orientationally resolved structure and dynamics in the isotropic sample. To isolate the anisotropic component, we exploit the fact that the INXS signal can be accurately decomposed [19,44,46–52] in terms of just the zeroth (isotropic) and second-order (anisotropic) Legendre polynomials with negligible higher-order contributions (Supplemental Material, Figs. 3 and 4 [15]). The ability to decompose the signal into the zeroth and second-order Legendre polynomials alone is consistent with what is expected for ISRS and the theory formulated in the Supplemental Material, Sec. I [15]. The middle and bottom rows of Fig. 1 show the anisotropic contribution to the INXS signal ( $\Delta S_2$ ) obtained from both experiment and molecular dynamics simulations (see Supplemental Material, Sec. IV [14,15,53–58]) of the theoretical treatment of INXS introduced here. The excellent agreement between the experimental and simulated  $\Delta S_2$  across the full time and scattering wave vector ( $q$ ) ranges probed demonstrates that the anisotropic component of the INXS signal can be accurately captured within linear response using our theoretical approach when combined with a polarizable force field treatment of chloroform.

To provide further insight into the time evolution of the anisotropic ( $\Delta S_2$ ) component of the INXS difference signal, Fig. 2 shows the scattering wave vector ( $q$ ) dependence of the signal for 1.2 ps following the initial excitation. Here the excellent agreement between the experiment and theory across the entire time range shown

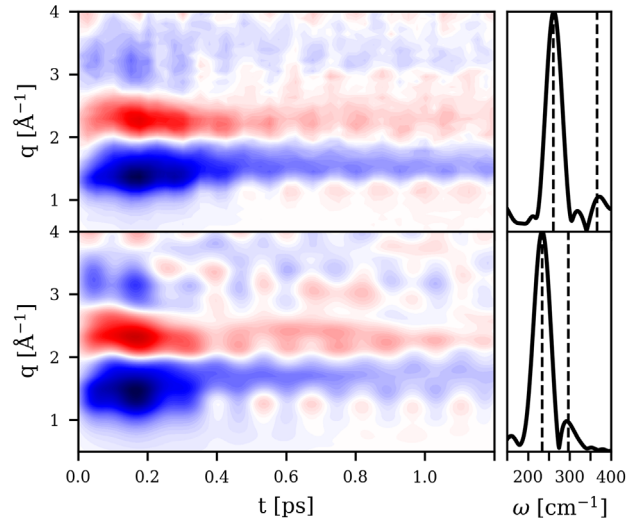


FIG. 2. The anisotropic component of the INXS signal,  $\Delta S_2(q, t)$ , from experiment (top left) and simulation (bottom left). Their Fourier transforms (right) show the temporal oscillations of the anisotropic component.

is even more evident with both exhibiting pronounced oscillatory features in the high  $q$  region while the low  $q$  region exhibits more nonoscillatory features indicative of diffusive dynamics. To elucidate the physical origins of these oscillatory features, the right-hand panel of Fig. 2 contains the frequency dependence of the principal component of the singular value decomposition of the anisotropic signal (see Supplemental Material, Sec. VIA [15]). From this we observe that the anisotropic signal has a large component at  $261 \text{ cm}^{-1}$  for the experiment and at  $234 \text{ cm}^{-1}$  for the simulation. The source of this frequency can be explained by considering the normal modes of the chloroform molecule (Supplemental Material, Table 1 [15,59–62]). Of chloroform's nine normal modes, six fall outside the current resolvable frequency range of the experiment ( $< 400 \text{ cm}^{-1}$ ), due to the temporal width of the excitation pulse. Of the three remaining normal modes, one is a doubly degenerate ( $e$  symmetry) vibration and appears at a frequency of  $261 \text{ cm}^{-1}$  with the other an ( $a_1$  symmetry) vibration at  $366 \text{ cm}^{-1}$  in the experimental Raman spectrum of the liquid [59]. We note that in the force field simulation, these modes appear in the Raman spectrum at  $234 \text{ cm}^{-1}$  and  $298 \text{ cm}^{-1}$  respectively (Supplemental Material, Fig. 5 [15]). The frequencies and symmetries of the intramolecular vibrations observed with INXS match the expectations established by polarized Raman scattering and ISRS. Specifically, the lower frequency asymmetric CCl bend ( $261 \text{ cm}^{-1}$ ,  $e$  symmetry) should predominantly appear in the anisotropic INXS signal, while the higher frequency symmetric CCl bend ( $366 \text{ cm}^{-1}$ ,  $a_1$  symmetry) should predominantly appear in the isotropic INXS signal [59]. The experimental and simulated INXS signals confirm these expectations (right panels of Fig. 2) that are further confirmed in the Supplemental Material, Fig. 8 [15], where the simulated INXS signal is Fourier transformed to the frequency domain. However, to understand the less oscillatory anharmonic intermolecular modes probed by the experiment it is useful to consider how the signal varies in time as a function of position.

To discern the more diffusive intermolecular contributions from the more oscillatory intramolecular contributions to the INXS signal, Fig. 3 shows the results of transforming both the isotropic and anisotropic components to real space where the spatial extent of these features helps identify their origins. Since chlorine atoms are by far the largest scatterers in this system, with an atomic form factor nearly threefold greater than that of the other atoms, one would expect the INXS signal to be dominated by chlorine-chlorine scattering. This is indeed the case in the simulations where, as demonstrated in the Supplemental Material, Fig. 9 [15], we can exactly extract the chlorine-chlorine contributions to the signal to leave only a small residual. By exploiting this realization, as shown in the Supplemental Material, Sec. VII [15], the transformation of

the experimental signal to real space and its physical interpretation can be simplified considerably.

While our primary focus is the physical interpretation of the anisotropic information that INXS reveals, it is instructive to first consider the content of the isotropic component. In particular, one can connect the isotropic component  $\Delta S_0(q, t)$  to the difference pair distribution function

$$\Delta g_{\text{ClCl}}^{(0)}(r, t) = 2 \int_0^\infty dq q^2 j_0(qr) \frac{\Delta S_0(q, t)}{F_{\text{Cl}}^*(q) F_{\text{Cl}}(q)} \quad (4a)$$

$$= \int_0^\pi d\varphi \sin \varphi \Delta g_{\text{ClCl}}(r, \varphi, t), \quad (4b)$$

where  $j_n$  is the  $n$ th order spherical Bessel function (see Supplemental Material, Sec. VII [15]). Equation (4b) introduces the well-known expression for the angular average over the polar angle  $\varphi$  (see Supplemental Material, Sec. VII [15]), which in the case of a conventional x-ray scattering signal corresponds to the circularly symmetric signal on the detector plane. Applying Eq. (4a) to the isotropic component of the simulated signal yields the difference pair distribution function shown in Fig. 3(e), where we see oscillations from the  $293 \text{ cm}^{-1}$  chloroform mode centered around the first intramolecular peak of  $g_{\text{ClCl}}(r)$ .

A similar transformation gives access to the real-space information contained in the anisotropic INXS signal. Specifically, we apply the second-order Bessel transformation to  $\Delta S_2(q, t)$ ,

$$\Delta g_{\text{ClCl}}^{(2)}(r, t) = -2 \int_0^\infty dq q^2 j_2(qr) \frac{\Delta S_2(q, t)}{F_{\text{Cl}}^*(q) F_{\text{Cl}}(q)} \quad (5a)$$

$$= \int_0^\pi d\varphi \sin \varphi \Delta g_{\text{ClCl}}(r, \varphi, t) P_2(\cos \varphi). \quad (5b)$$

By comparing the expression in Eq. (5b) to the expression for the standard difference pair distribution function in Eq. (4b) and noting that  $P_0[\cos(\varphi)] = 1$ , we see that this procedure yields a difference generalized pair distribution function that encapsulates the angularly resolved fluctuations of the distribution following the symmetry of the second-order Legendre polynomial  $P_2[\cos(\varphi)]$ .  $\Delta g_{\text{ClCl}}^{(2)}(r, t)$  thus provides a direct measure of fluctuations in the projection of the pair distribution onto the anisotropic polarizability. This anisotropic component of the INXS signal mirrors the symmetry of the second-order Legendre polynomial, which displays a pattern with two pairs of positive and negative lobes around the circle, and when fully averaged across the circle would disappear. This additional information expands on that provided by conventional x-ray and neutron scattering experiments which only provide the isotropic averaging shown in Eq. (4b). The transformation of the simulated  $\Delta S_2(q, t)$  to real space,

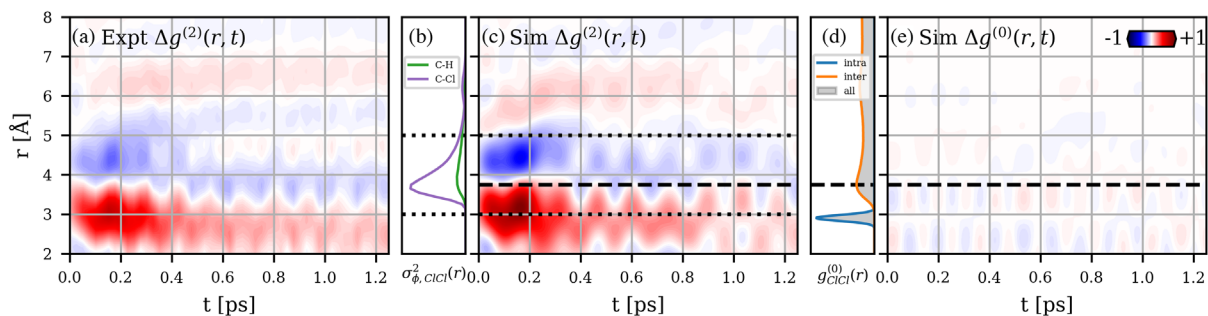


FIG. 3. The real-space transformed anisotropic component of the INXS signal,  $\Delta g^{(2)}(r, t)$ , from (a) experiment and (c) simulation. (b) Simulated variance arising from angular fluctuations at each distance along the C-H and C-Cl axes. Comparing  $\Delta g^{(2)}(r, t)$  in (c) with the simulated chlorine-chlorine radial distribution function  $g_{\text{ClCl}}(r)$  in (d) demonstrates the anisotropic nonoscillatory component is intermolecular in character since it straddles the first intermolecular (orange) peak in  $g^{(0)}(r)$  but is absent from the isotropic component  $\Delta g^{(0)}(r, t)$  shown in (e).

$\Delta g^{(2)}(r, t)$ , as shown in Fig. 3(c) allows us to determine the origins of the nonoscillatory features in the signal. For example, the nonoscillatory feature that peaks at  $\sim 200$  fs and subsequently decays straddles the first intermolecular chlorine-chlorine peak of the simulated  $g_{\text{ClCl}}(r)$  centered at  $3.75 \text{ \AA}$ . This suggests that it arises from motions following excitation that lead to purely intermolecular redistribution, which is consistent with observations from optical Kerr effect measurements [11,63]. This is confirmed in the Supplemental Material, Fig. 10 [15], where we exactly decompose the simulated INXS signal into its intramolecular and intermolecular components where the intramolecular component lacks this feature. In contrast, this nonoscillatory intermolecular peak does not appear in the isotropic signal. Hence, the Raman excitation causes an anisotropic orientational rearrangement of neighboring chloroform molecules (angularly distributed according to the second-order Legendre polynomial) that conserves the average intermolecular chlorine-chlorine distance.

To provide insight into the local molecular arrangements that lead to the nonoscillatory positive and negative feature at  $\sim 200$  fs in the region  $3\text{--}5 \text{ \AA}$  in  $\Delta g^{(2)}(r, t)$ , we consider the density fluctuations of chlorine that dominate the anisotropic response in the real space INXS signal. Since  $g^{(2)}(r, t)$  arises from anisotropic orientational rearrangements, the experimental signal at a particular distance  $r$  is sensitive to the variance of the angular distribution [Fig. 3(b)] at that distance, i.e., if there is no angular variation in the molecular density at that distance, the signal will be isotropic and will not contribute to  $\Delta g^{(2)}(r, t)$ . Figure 3(b) shows the variance of the angular distribution of the chlorine-chlorine radial distribution function along the two principal symmetry axes of the chloroform molecule: the C-H axis and the Cl-C-Cl bisector perpendicular to the C-H axis (see Supplemental Material, Sec. X [15]), which are also the principal axes of chloroform's molecular polarizability tensor [64]. From this, one can see that for both axes the variance of the angular distribution is largest

in the region  $3\text{--}5 \text{ \AA}$  consistent with the regions of the greatest signal in  $g^{(2)}(r, t)$  [dotted lines in Fig. 3(c)]. This can be seen even more clearly in the Supplemental Material, Fig. 10 [15], where we show just the intermolecular  $\Delta g^{(2)}(r, t)$  obtained from the simulations.

Thus, by breaking the symmetry of an isotropic sample through the directionality of a Raman interaction, the real-space anisotropic INXS signal reveals an angularly resolved microscopic density and orientational fluctuations in chemical, biological, and materials systems with fs and  $\text{\AA}$  level resolution as a response to an impulsive excitation. The theoretical and simulation framework presented here offers the opportunity to obtain and understand the unique orientational structure and dynamical information about the molecular to nanoscopic structure of liquids and glasses present in experiments that harness optically induced anisotropy in time-resolved scattering.

This work was supported by the U.S. Department of Energy, Office of Science, Basic Energy Sciences, Chemical Sciences, Geosciences, and Biosciences Division. The authors wish to acknowledge LCLS staff including T. Sato, J. Glowia, D. Zhu, S. Nelson, and A. Robert for experimental support and helpful discussions. Use of the Linac Coherent Light Source (LCLS), SLAC National Accelerator Laboratory, is supported by the U.S. Department of Energy, Office of Science, Office of Basic Energy Sciences under Contract No. DE-AC02-76SF00515. Initial development of analytical theory was supported by the Department of Energy, Laboratory Directed Research and Development program at SLAC National Accelerator Laboratory, under Contract No. DE-AC02-76SF00515. This research used resources of the National Energy Research Scientific Computing Center (NERSC), a U.S. Department of Energy Office of Science User Facility operated under Contract No. DE-AC02-05CH11231.

\*kgaffney@slac.stanford.edu

†timbvd@slac.stanford.edu

‡tmarkland@stanford.edu

- [1] S. Mukamel, *Principles of Nonlinear Optical Spectroscopy* (Oxford University Press, New York, 1995).
- [2] F. Sette, M. H. Krisch, C. Masciovecchio, G. Ruocco, and G. Monaco, *Science* **280**, 1550 (1998).
- [3] J. Teixeira, M. C. Bellissent-Funel, S. H. Chen, and B. Dorner, *Phys. Rev. Lett.* **54**, 2681 (1985).
- [4] J. Teixeira, M. C. Bellissent-Funel, S. H. Chen, and A. J. Dianoux, *Phys. Rev. A* **31**, 1913 (1985).
- [5] J. G. Kim, E. H. Choi, Y. Lee, and H. Ihee, *Acc. Chem. Res.* **54**, 1685 (2021).
- [6] M. Chergui and E. Collet, *Chem. Rev.* **117**, 11025 (2017).
- [7] K. J. Gaffney, *Chem. Sci.* **12**, 8010 (2021).
- [8] E. Biasin *et al.*, *Nat. Chem.* **13**, 343 (2021).
- [9] P. Vohringer and N. F. Scherer, *J. Phys. Chem.* **99**, 2684 (1995).
- [10] L. Dhar, J. A. Rogers, and K. A. Nelson, *Chem. Rev.* **94**, 157 (1994).
- [11] B. J. Loughnane, A. Scodinu, R. A. Farrer, J. T. Fourkas, and U. Mohanty, *J. Chem. Phys.* **111**, 2686 (1999).
- [12] H. Ki, S. Choi, J. Kim, E. H. Choi, S. Lee, Y. Lee, K. Yoon, C. W. Ahn, D.-S. Ahn, J. H. Lee, J. Park, I. Eom, M. Kim, S. H. Chun, J. Kim, H. Ihee, and J. Kim, *J. Am. Chem. Soc.* **143**, 14261 (2021).
- [13] K. H. Kim *et al.*, *Phys. Rev. Lett.* **125**, 076002 (2020).
- [14] X. Mu, Q. Wang, L. P. Wang, S. D. Fried, J. P. Piquemal, K. N. Dalby, and P. Ren, *J. Phys. Chem. B* **118**, 6456 (2014).
- [15] See Supplemental Material at <http://link.aps.org/supplemental/10.1103/PhysRevLett.129.056001> for details on the derivation of the theory, the experimental setup, the simulation, and analyses of the experimental and simulation data.
- [16] S. Tanaka, V. Chernyak, and S. Mukamel, *Phys. Rev. A* **63**, 063405 (2001).
- [17] J. Als-Nielsen and D. McMorrow, *Elements of Modern X-Ray Physics* (John Wiley & Sons, Ltd, New York, 2011).
- [18] B. J. Berne and G. D. Harp, On the calculation of time correlation functions, in *Advances in Chemical Physics* (John Wiley & Sons, Ltd, New York, 1970), pp. 63–227.
- [19] M. Ben-Nun, J. Cao, and K. R. Wilson, *J. Phys. Chem. A* **101**, 8743 (1997).
- [20] J. Cao and K. R. Wilson, *J. Phys. Chem. A* **102**, 9523 (1998).
- [21] M. Cho, G. R. Fleming, and S. Mukamel, *J. Chem. Phys.* **98**, 5314 (1993).
- [22] P. Coppens, *Annu. Rev. Phys. Chem.* **43**, 663 (1992).
- [23] D. P. Craig and T. Thirunamachandran, *Molecular Quantum Electrodynamics* (Academic Press Inc., Orlando, Florida, 1984).
- [24] I. R. Craig and D. E. Manolopoulos, *J. Chem. Phys.* **121**, 3368 (2004).
- [25] I. R. Craig and D. E. Manolopoulos, *J. Chem. Phys.* **122**, 084106 (2005).
- [26] G. Dixit, O. Vendrell, and R. Santra, *Proc. Natl. Acad. Sci. U.S.A.* **109**, 11636 (2012).
- [27] A. O. Dohn, E. Biasin, K. Haldrup, M. M. Nielsen, N. E. Henriksen, and K. B. Møller, *J. Phys. B* **48** (2015).
- [28] S. A. Egorov, K. F. Everitt, and J. L. Skinner, *J. Phys. Chem. A* **103**, 9494 (1999).
- [29] *Time-Resolved Diffraction*, edited by J. R. Helliwell and P. M. Rentzepis (Clarendon Press, Oxford, 1997).
- [30] D. A. Long, *The Raman Effect: A Unified Treatment of the Theory of Raman Scattering by Molecules* (John Wiley & Sons, Ltd, New York, 2002).
- [31] S. Luber, M. Iannuzzi, and J. Hutter, *J. Chem. Phys.* **141**, 094503 (2014).
- [32] K. B. Møller and N. E. Henriksen, in *Molecular Electronic Structures of Transition Metal Complexes I*, edited by D. M. P. Mingos, P. Day, and J. P. Dahl (Springer Berlin Heidelberg, Berlin, Heidelberg, 2012), pp. 185–211.
- [33] A. Moreno Carrascosa, T. Northey, and A. Kirrander, *Phys. Chem. Chem. Phys.* **19**, 7853 (2017).
- [34] A. Moreno Carrascosa, H. Yong, D. L. Crittenden, P. M. Weber, and A. Kirrander, *J. Chem. Theory Comput.* **15**, 2836 (2019).
- [35] T. Northey, N. Zotev, and A. Kirrander, *J. Chem. Theory Comput.* **10**, 4911 (2014).
- [36] T. Northey, A. Moreno Carrascosa, S. Schäfer, and A. Kirrander, *J. Chem. Phys.* **145**, 154304 (2016).
- [37] G. Pálinkás, *Acta Cryst.* **A29**, 10 (1973).
- [38] R. Ramírez, T. López-Ciudad, P. Kumar P, and D. Marx, *J. Chem. Phys.* **121**, 3973 (2004).
- [39] T. Rozgonyi, R. Sauerbrey, and T. Feurer, *J. Appl. Phys.* **97**, 013537 (2005).
- [40] A. K. Soper, *J. Phys. Condens. Matter* **19**, 335206 (2007).
- [41] Y. Tanimura and S. Mukamel, *J. Chem. Phys.* **99**, 9496 (1993).
- [42] Y. J. Yan and S. Mukamel, *J. Chem. Phys.* **94**, 997 (1991).
- [43] P. Hart *et al.*, *X-Ray Free-Electron Lasers: Beam Diagnostics, Beamline Instrumentation, and Applications* (SPIE, 2012), Vol. 8504, p. 85040C.
- [44] E. Biasin, T. B. van Driel, G. Levi, M. G. Laursen, A. O. Dohn, A. Moltke, P. Vester, F. B. K. Hansen, K. S. Kjaer, T. Harlang, R. Hartsock, M. Christensen, K. J. Gaffney, N. E. Henriksen, K. B. Møller, K. Haldrup, and M. M. Nielsen, *J. Synchrotron Radiat.* **25**, 306 (2018).
- [45] K. S. Kjaer, T. B. Van Driel, J. Kehres, K. Haldrup, D. Khakhulin, K. Bechgaard, M. Cammarata, M. Wulff, T. J. Sørensen, and M. M. Nielsen, *Phys. Chem. Chem. Phys.* **15**, 15003 (2013).
- [46] A. Natan, A. Schori, G. Owolabi, J. P. Cryan, J. M. Glowonia, and P. H. Bucksbaum, *Faraday Discuss.* **228**, 123 (2021).
- [47] E. Biasin *et al.*, *Phys. Rev. Lett.* **117**, 013002 (2016).
- [48] K. S. Kjaer *et al.*, *Chem. Sci.* **10**, 5749 (2019).
- [49] U. Lorenz, K. B. Møller, and N. E. Henriksen, *New J. Phys.* **12** (2010).
- [50] J. S. Baskin and A. H. Zewail, *Chem. Phys. Chem.* **7**, 1562 (2006).
- [51] J. S. Baskin and A. H. Zewail, *Chem. Phys. Chem.* **6**, 2261 (2005).
- [52] E. H. Van Kleef and I. Powis, *Mol. Phys.* **96**, 757 (1999).
- [53] J. Ponder, TINKER—Software tools for molecular design, V. 6.3.3, Saint Louis, (2004).
- [54] J. W. Ponder, C. Wu, P. Ren, V. S. Pande, J. D. Chodera, M. J. Schnieders, I. Haque, D. L. Mobley, D. S. Lambrecht,

- R. A. Distasio, M. Head-Gordon, G.N. Clark, M.E. Johnson, and T. Head-Gordon, *J. Phys. Chem. B* **114**, 2549 (2010).
- [55] L. Martínez, R. Andrade, E. Birgin, and J. Martínez, *J. Comput. Chem.* **30**, 2157 (2009).
- [56] Z. Atik, *J. Chem. Eng. Data* **52**, 1128 (2007).
- [57] G. Bussi, D. Donadio, and M. Parrinello, *J. Chem. Phys.* **126**, 014101 (2007).
- [58] U. Essmann, L. Perera, M. L. Berkowitz, T. Darden, H. Lee, and L. G. Pedersen, *J. Chem. Phys.* **103**, 8577 (1995).
- [59] J. R. Madigan and F. F. Cleveland, *J. Chem. Phys.* **19**, 119 (1951).
- [60] T. Shimanouchi, in *Tables of Molecular Vibrational Frequencies Consolidated Volume I* (National Bureau of Standards, Washington, DC, 1972), pp. 1–160.
- [61] J. Rud Nielsen and N.E. Ward, *J. Chem. Phys.* **10**, 81 (1942).
- [62] T. G. Gibian and D. S. McKinney, *J. Am. Chem. Soc.* **73**, 1431 (1951).
- [63] N. T. Hunt, A. A. Jaye, and S. R. Meech, *Phys. Chem. Chem. Phys.* **9**, 2167 (2007).
- [64] F. D. Vila, D. A. Strubbe, Y. Takimoto, X. Andrade, A. Rubio, S. G. Louie, and J. J. Rehr, *J. Chem. Phys.* **133**, 034111 (2010).